Chemical Science

ROYAL SOCIETY OF CHEMISTRY

EDGE ARTICLE

View Article Online
View Journal

Check for updates

Cite this: DOI: 10.1039/d6sc02442d

All publication charges for this article have been paid for by the Royal Society of Chemistry

Molten-salt flash synthesis of P-doped iron oxide with engineered oxygen vacancies for lattice-oxygen water oxidation

Jiahui Luo,[ab] Baoxin Wu,[ac] Kejun Yan,[ab] Yongbiao Mu,[ab] Qing Zhang,[ab] Huanxiu Zou,[d] Zhiqing Tang,[ab] Guobin Zhang,[e] Wanwisa Limphirat,[f] Wenjia Li*[ab] and Lin Zeng*[ab]

Received 25th March 2026
Accepted 21st May 2026

DOI: 10.1039/d6sc02442d

rsc.li/chemical-science

Industrial anion exchange membrane water electrolysis (AEMWE) still lacks earth-abundant oxygen evolution reaction (OER) catalysts that simultaneously exhibit high intrinsic activity and long-term durability. This limitation mainly originates from the conventional adsorbate evolution mechanism (AEM), which is restricted by the linear scaling relationship between *OOH and *O intermediates. Herein, we propose a rapid diffusion strategy based on molten-salt-assisted approach to synthesize P/FeO$_x$. The entire synthesis completes within minutes *via* high-temperature solid-state interdiffusion, enabling single-batch production at the kilogram scale with exceptional time and energy efficiency. Phosphorus doping successfully narrows the band gap between Fe 3d and O 2p, thus enhancing electronic conductivity. It also promotes the formation of O$_v$ and induces a mechanistic transition from the AEM to the lattice-oxygen oxidation mechanism (LOM) pathway, simultaneously reducing the activation barrier for the *OH → *O step. The optimized catalyst achieves an overpotential of 256 mV at 100 mA cm^{-2} and maintains stable operation for over 2000 h at 100 mA cm^{-2} without noticeable degradation. When integrated into an AEMWE device, the membrane-electrode assembly requires merely 1.78 V to deliver 500 mA cm^{-2} and operates stably for 1000 h. In conclusion, this study presents a rational synthesis approach and practical design principles for engineering high-performance OER electrocatalysts tailored to industrial water electrolysis.

Introduction

Anion exchange membrane water electrolysis (AEMWE) powered by intermittent solar or wind energy provides a direct pathway to green hydrogen production while mitigating renewable power fluctuations and simplifying the balance of the system.[1–3] However, the anodic oxygen evolution reaction (OER) in AEMWE involves sluggish kinetics due to the complex four-electron transfer process, severely limiting the overall conversion efficiency. This reaction requires large overpotentials and often leads to anode degradation caused by excessive lattice oxygen release.[4–7] Currently, state-of-the-art anodes still rely on noble-metal-based catalysts (*e.g.*, Ru and Ir) because they exhibit the lowest overpotentials and acceptable durability at potentials above 1.6 V *vs.* the reversible hydrogen electrode.[8] Nevertheless, their scarcity results in high and unstable costs, and under high anodic bias (>1.6 V), both Ir and Ru tend to dissolve into IrO_4^{2-} or RuO_4^{2-} species, which can migrate through the membrane and poison the cathode. Consequently, earth-abundant 3d transition metal oxides (TMOs), particularly those based on Fe, Co, Ni, and Mn, are being actively explored as cost-effective and scalable alternatives for AEMWE anodes.[9–12] Among them, iron oxide stands out as one of the most stable, inexpensive, and environmentally benign TMOs, and it has been extensively investigated as a light absorber for water oxidation. However, its interfacial hole-extraction kinetics remain sluggish.[4,13–16] To accelerate hole transfer, various strategies, including electronic spin modulation,[17,18] adsorption energy tuning,[19] lattice oxygen activation,[20,21] heterojunction regulation,[22] and conductivity enhancement,[23,24] have been developed through elemental doping, defect engineering, and support coupling.[25,26] In particular, elemental doping (*e.g.*, with S, P, or Ru) offers a simple and scalable approach to tailor metal–oxygen

---

[a] Department of Mechanical and Energy Engineering, Southern University of Science and Technology, Shenzhen 518055, China

[b] SUSTech Energy Institute for Carbon Neutrality, Southern University of Science and Technology, Shenzhen 518055, P. R. China

[c] Department of Mechanical Engineering, The Hong Kong Polytechnic University, Hung Hom, Kowloon, Hong Kong SAR, P. R. China

[d] Key Laboratory of Hunan Province for Advanced Carbon-Based Functional Materials, School of Chemistry and Chemical Engineering, Hunan Institute of Science and Technology, Yueyang 414006, P. R. China

[e] Future Technology School, Shenzhen Technology University, Shenzhen, 518118, China

[f] Synchrotron Light Research Institute, 111 University Avenue, Muang District, Nakhon Ratchasima 30000, Thailand

covalency and shift the Fermi level, thereby facilitating charge transfer and weakening surface–adsorbate interactions. Unlike complex heterostructure design, doping introduces no additional interfacial resistance and can be readily integrated into existing catalyst synthesis processes.[27–30]

Extensive studies have demonstrated that the intrinsic oxygen evolution reaction (OER) activity of an electrocatalyst is primarily determined by the reaction pathway occurring at its active sites.[31,32] In alkaline media, the OER process generally proceeds through two main pathways: the adsorbate evolution mechanism (AEM) and the lattice oxygen mechanism (LOM).[19,33] In the conventional AEM process, the catalytic performance is governed by the binding strength of metal sites toward oxygenated intermediates, including *OH, *O, and *OOH. However, this pathway is inherently limited by the linear *OOH–*O scaling relationship, which constrains the theoretical overpotential to approximately 0.37 V. In contrast, the LOM bypasses the *OOH formation bottleneck by coupling *O with lattice oxygen to form O_2, thereby achieving a lower theoretical overpotential.[34] Consequently, regulating the reaction pathway through electronic structure modulation and surface engineering provides an effective strategy to lower the overall overpotential. A key characteristic of the LOM pathway is the absence of the *OOH intermediate; lattice oxygen participates directly in forming *OO species, circumventing the potential-determining O–O coupling step and minimizing both overpotential and energy loss.[35] As a result, LOM-based electrocatalysts have emerged as a central research focus in water-splitting catalysis.[36–38] For instance, Huang *et al.*[39] employed ^{18}O differential electrochemical mass spectrometry (DEMS) and density functional theory (DFT) analyses to reveal that abundant oxygen vacancies in Fe_2O_3–CeO_2 heterojunctions facilitate a mechanistic transition from the AEM to LOM. Similarly, Tang *et al.*[40] demonstrated that atomic-scale incorporation of rare-earth elements into $NiCo_2O_4$ enhances M–O covalency, thereby activating lattice oxygen. Both experimental and theoretical investigations consistently indicate that a vacancy-rich transition-metal (oxy)hydroxide matrix with strengthened M–O covalency is a prerequisite for efficient lattice-oxygen oxidation in transition-metal oxides.[34,41–44]

Molten-salt-assisted synthesis has recently emerged as an effective strategy for modulating the morphology and microstructure of catalysts.[45–47] Although phosphorus incorporation can, in principle, be realized by conventional synthetic or post-treatment methods, such routes usually involve relatively slow diffusion processes and may lead to less controllable dopant distribution, limited defect regulation, or particle aggregation. In contrast, the molten-salt flash synthesis strategy provides a highly dynamic and non-equilibrium reaction environment, where rapid ion diffusion and efficient mass transport enable simultaneous surface-confined phosphorus incorporation, oxygen-vacancy generation, and morphology regulation within a short reaction time. Therefore, the optimized catalytic behavior of P/FeO_x originates from the synergistic effect between phosphorus-induced electronic/defect modulation and the unique structural regulation enabled by the molten-salt flash synthesis route.[48] In this work, we developed a rapid diffusion strategy based on a molten-salt-assisted approach to construct an iron oxide catalyst with *in situ* phosphorus doping. With high-temperature solid-state interdiffusion, we achieved simultaneous morphology regulation and oxygen-vacancy engineering. The molten-salt-mediated rapid annealing effectively relieves lattice strain and introduces multidimensional vacancies into the Fe_2O_3 matrix. Phosphorus incorporation downshifts the Fe 3d conduction band, narrows the bandgap, and thereby enhances electronic conductivity. Comprehensive characterization techniques, including electron paramagnetic resonance (EPR), pH-dependent activity measurements, TMAOH probing experiments, *operando* ^{18}O-labeled DEMS, and DFT calculations, suggest that phosphorus incorporation promotes lattice-oxygen activation and enhances the contribution of catalyst-derived oxygen species during the OER. Rather than indicating a complete AEM-to-LOM transition, these results support a LOM-involved pathway with partial lattice-oxygen participation in P/FeO_x. The optimized catalyst achieves overpotentials of only 208 and 256 mV at current densities of 10 and 100 mA cm^{-2}, respectively, and demonstrates exceptional durability over 2000 h. When assembled into an alkaline AEMWE device, it delivers 500 mA cm^{-2} at 1.78 V (60 °C) and maintains stable operation for 1000 h without observable degradation. In summary, this work establishes a molten-salt-assisted protocol that merges facile operation with kilogram-scale throughput, leveraging the high-ion-conductivity melt to collapse diffusion barriers and accelerate reaction kinetics. It delivers practical design rules for the rapid deployment of high-activity, robust oxygen-evolution electrocatalysts in industrial water electrolysis.

Results and discussion

We employed a molten-salt-assisted synthesis to prepare a phosphorus-doped iron oxide catalyst (denoted as P/FeO_x) at high temperature (Fig. 1a). A stoichiometric mixture of NaH_2PO_4, $FeCl_2$ and $NaNO_3$ was ground and rapidly introduced into molten $NaNO_3$. The instantaneous addition of NaH_2PO_4 and $FeCl_2$ maximized the interfacial contact between phosphorus and Fe^{2+} species, while flash heating and cooling efficiently promoted the formation of amorphous phases. Within three minutes, phosphorus atoms stabilized the oxygen vacancies (V_O) generated during the molten-salt reaction, yielding a nanocrystalline solid powder (P/FeO_x). The entire synthesis was completed within minutes, and its high-ion-conductivity molten-salt environment simultaneously suppressed diffusion limitations and enabled facile morphology control, ensuring rapid, energy-efficient production of electrocatalysts directly applicable to industrial water electrolysis.

Scanning electron microscopy (SEM) revealed that the phosphorus-rich oxide exhibited a number-weighted particle diameter of 50–100 nm, markedly smaller than that of its undoped counterpart (100–300 nm; Fig. S1 and S2, SI). Besides, laser particle size analysis (LPSA) further confirmed that phosphorus doping effectively reduced the average particle size and suppressed grain growth (Fig. S3, SI). Powder X-ray diffraction (XRD) was performed to examine the phase structure of P/FeO_x.

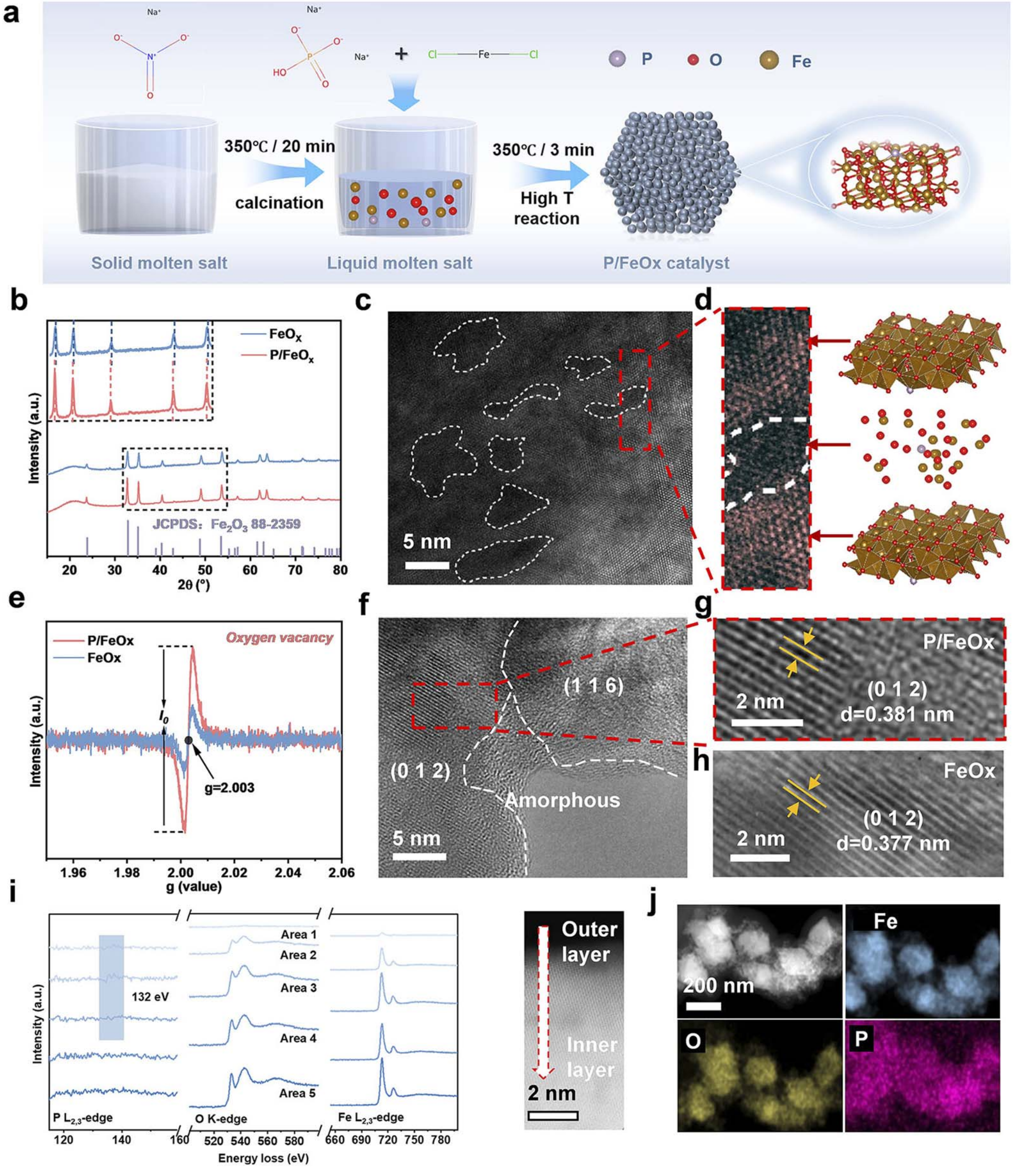

Fig. 1 (a) Schematic illustration of the synthesis of the P/FeO$_x$ catalyst. (b) Powder X-ray diffraction patterns of P/FeO$_x$ and its reference sample. (c) HAADF-STEM image and (d) its partial enlarged view of P/FeO$_x$. (e) Electron paramagnetic resonance spectra of P/FeO$_x$ and FeO$_x$. (f)–(h) High-resolution transmission electron microscopy images of P/FeO$_x$ and FeO$_x$. (i) Electron energy-loss spectroscopy (EELS) line-scan of P/FeO$_x$. (j) Energy dispersive spectrometry images of P/FeO$_x$.

As shown in Fig. 1b, the diffraction peaks located at 2θ values of 23.7°, 32.7°, 35.2°, 49.1°, 53.7°, 62.1°, and 63.7° can be indexed to hematite Fe_2O_3 (JCPDS No. 88-2359). Compared with FeO$_x$, P/FeO$_x$ exhibits slight peak broadening and a small shift toward lower 2θ angles, suggesting increased interplanar spacing and possible lattice expansion/strain after phosphorus incorporation. The aberration-corrected high-angle annular dark-field scanning TEM (AC-HAADF-STEM) analysis of P/FeO$_x$ revealed abundant crystalline–amorphous (c–a) interfaces (Fig. 1c, S4 and S5). Besides, further analysis clearly indicated the interlaced crystalline and amorphous structure (Fig. 1d), simply due to the flash heating and cooling process of the molten-salt reaction. To study the composition of the amorphous phase, electron paramagnetic resonance (EPR) spectroscopy was further employed to probe the concentration of oxygen vacancies (V_O) in the catalysts (Fig. 1e). P/FeO$_x$ displayed a significantly intensified EPR signal compared with the undoped FeO$_x$, confirming the enhanced formation of V_O induced by phosphorus incorporation. These results collectively demonstrate the superior oxygen-vacancy-generating ability of phosphorus and its critical role in boosting OER performance. When focused on the crystal phase in the catalyst, high-resolution transmission electron microscopy (HRTEM) images showed that the FeO$_x$ particles were well faceted, while phosphorus incorporation disrupted the long-range order and produced an amorphous surface layer enriched with coordinatively unsaturated Fe sites (Fig. 1f, S6 and S7, SI).

In addition to the amorphous halo (Fig. 1f), lattice fringes corresponding to the (116) and (112) planes of P/FeO$_x$ were clearly identified. The lattice spacing of the (112) facet expanded from 0.377 nm in FeO$_x$ to 0.381 nm upon phosphorus incorporation (Fig. 1g and h), evidencing lattice strain associated with phosphorus enrichment. Furthermore, the phosphorus distribution in P/FeO$_x$ was investigated by electron energy-loss spectroscopy (EELS) line-scan across an individual particle. As shown in Fig. 1i, the P L$_{2,3}$-edge signal is mainly detected within the first ∼2.0 nm from the surface and gradually decreases to the noise level at greater depths, whereas the Fe L$_{2,3}$-edge and O K-edge signals remain relatively constant across the scanned region. These results indicate that phosphorus species are predominantly confined to the surface/near-surface region rather than being uniformly incorporated into the bulk lattice. Such a surface-confined distribution exposes P-modified Fe–O sites directly to the electrolyte, which is favorable for regulating the near-surface electronic structure, oxygen-vacancy formation, and interfacial OER kinetics. Elemental mapping by energy-dispersive X-ray spectroscopy (EDS) further confirmed the uniform distribution of Fe, P, and O within the nanoparticles (Fig. 1j and S8, SI), indicating a homogeneous single-phase structure. Quantitative analysis revealed approximate atomic contents of 3.29 at% P, 30.40 at% Fe, and 66.31 at% O (Table S1, SI). In addition, the Raman spectra of P/FeO$_x$ and FeO$_x$ exhibited seven characteristic phonon modes of Fe$_2$O$_3$ at 223, 238, 291, 408, 499, 609, and 657 cm^{-1} (Fig. S9, SI), corroborating the above XRD results. ICP-OES was further performed to quantify the actual phosphorus content in the final catalysts. For the optimized P/FeO$_x$ sample prepared with a nominal phosphorus feeding ratio of 2 wt%, the actual phosphorus content is 0.84 wt%, corresponding to a phosphorus retention efficiency of approximately 42%. The lower actual content than the nominal feeding amount suggests that part of the introduced phosphorus is removed during molten-salt synthesis and subsequent washing. These results provide quantitative information on the retained phosphorus content in P/FeO$_x$ and clarify the relationship between the precursor feeding amount and the actual catalyst composition.

X-ray photoelectron spectroscopy (XPS) was employed to probe the surface chemical states and near-surface electronic environment of the catalysts. Therefore, the Fe 2p and O 1s spectra are discussed mainly in terms of surface electronic modulation and surface oxygen-vacancy-related species. As shown in Fig. S10, SI, the peak located at approximately 133 eV corresponds to the P 2p signal, confirming the successful

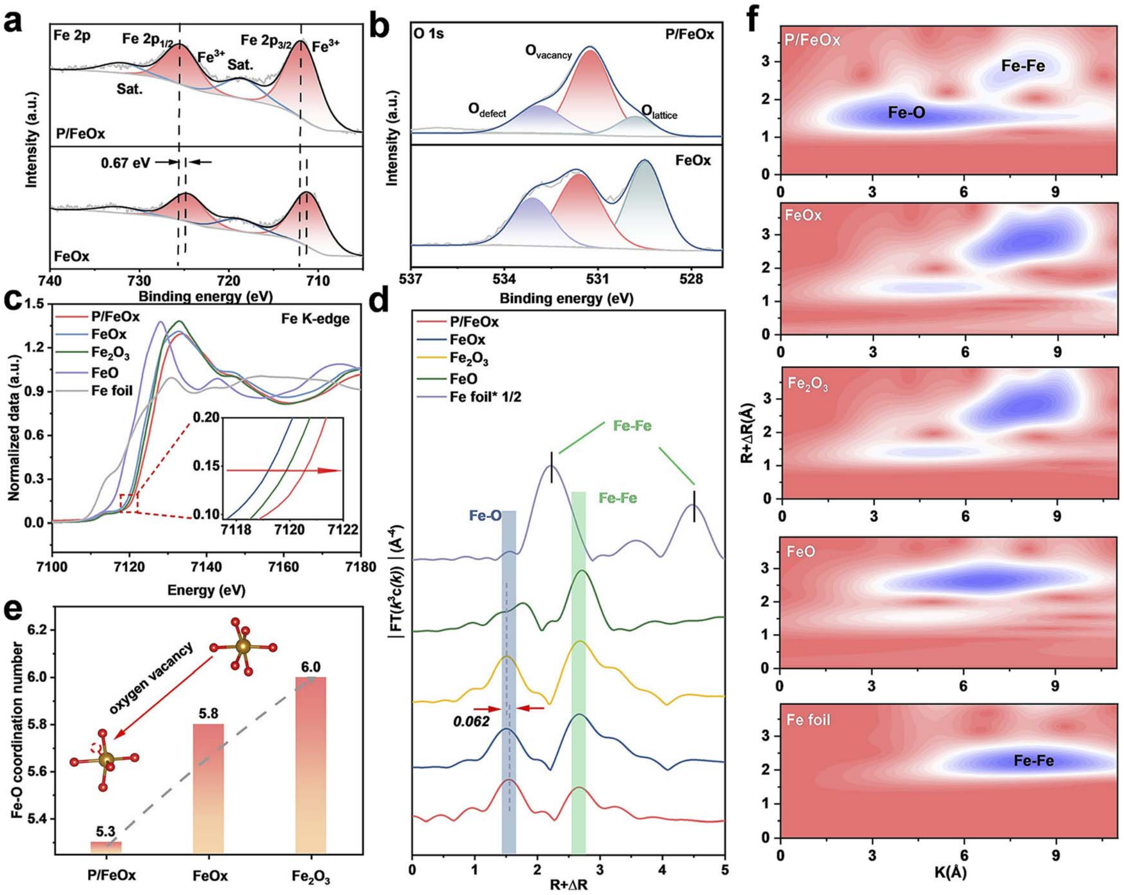

Fig. 2 X-ray photoelectron spectroscopy (XPS) spectra of (a) Fe 2p and (b) O 1s of the samples. (c) Fe K-edge XANES spectra and (d) Fourier-transformed k^2-weighted magnitudes of the EXAFS signals of the samples. (e) Fe–O coordination number obtained by fitting curves from Fourier-transformed k^3-weighted EXAFS spectra. (f) Fe k-edge wavelet-transformed (WT) EXAFS spectra of the samples.

incorporation of phosphorus. The Fe 2p spectra of P/FeO$_x$ and FeO$_x$ are displayed in Fig. 2a. The characteristic peaks at 712.0/725.5 eV and 718.6/732.1 eV were assigned to Fe^{3+} (2p$_{3/2}$/2p$_{1/2}$) and their corresponding satellite peaks, respectively. Compared with FeO$_x$, the Fe 2p peaks of P/FeO$_x$ shift slightly toward higher binding energy, indicating that phosphorus incorporation modifies the local electronic environment of Fe species. This shift reflects electronic redistribution within the Fe–O–P framework. As shown in Fig. 2b, the O 1s spectra were deconvoluted into three distinct components corresponding to O$_{\text{lattice}}$, O$_{\text{vacancy}}$, and O$_{\text{defect}}$. The O$_{\text{lattice}}$ peak at ∼529.7 eV is associated with oxygen bound within the metal oxide lattice, while the O$_{\text{vacancy}}$ peak centered at ∼531.2 eV arises from surface chemisorbed oxygen species (O_2^{2-} or O^-) linked to defect oxides or hydroxyl groups. The O$_{\text{defect}}$ component is attributed to unavoidable surface contaminants such as residual water and carbon–oxygen species from adsorbed organics. The ratio of O$_{\text{vacancy}}$/O$_{\text{lattice}}$ serves as a qualitative indicator of surface oxygen-vacancy concentration, where a higher ratio corresponds to a greater vacancy density. As illustrated in Fig. 2b, FeO$_x$ exhibits a relatively low O$_{\text{vacancy}}$/O$_{\text{lattice}}$ ratio, while the ratio increases markedly in P/FeO$_x$, indicating that P–O bonding effectively promotes the generation of surface oxygen vacancies.

To further investigate the average electronic structure and local coordination environment of Fe atoms, X-ray absorption spectroscopy (XAS) measurements were performed. The Fe K-edge XANES spectra provide information on the average oxidation state and electronic structure of Fe, while the EXAFS fitting results reveal the average Fe–O coordination environment, including the Fe–O coordination number and local structural disorder. The normalized Fe K-edge X-ray absorption near-edge structure (XANES) spectra of P/FeO$_x$, and FeO$_x$ closely resemble that of Fe$_2$O$_3$ (Fig. 2c), confirming that Fe species predominantly exist in a positively charged state with an average oxidation state near +3. The oxidation states of P/FeO$_x$ (+3.05) and FeO$_x$ (+2.83) were calculated by linearly fitting the first derivative position (E_0) (Fig. S12, SI). The increased Fe valence is mainly attributed to electron aggregation around phosphorus. Fourier-transformed extended X-ray absorption fine structure (FT-XANES) spectra at the Fe K-edge (Fig. 2d) show peaks at approximately 1.54 and 2.67 Å, corresponding to Fe–O and Fe–Fe coordination, respectively, consistent with Fe$_2$O$_3$. Upon phosphorus incorporation, the Fe–O bond length shifts to higher R values by ∼0.062 Å, reflecting lattice expansion due to substitutional incorporation of larger P atoms for O atoms. The EXAFS fitting results (Fig. S13 and Table S2, SI) indicate Fe–O coordination numbers of 6.00, 5.85, and 5.31 for Fe$_2$O$_3$, FeO$_x$, and P/FeO$_x$, respectively. Compared with FeO$_x$, the further decrease in the Fe–O coordination number of P/FeO$_x$ suggests that phosphorus incorporation induces a more defective and disordered local Fe–O environment. Considering that both FeO$_x$ and P/FeO$_x$ were synthesized by the same molten-salt route, this additional reduction in coordination number indicates that phosphorus doping introduces extra perturbation to the Fe–O framework during oxide formation, leading to enhanced defect generation and local structural distortion in the catalyst. Besides, the corresponding k-space fitting curves (Fig. S14, SI) further validate the reliability of these results. Wavelet-transformed (WT) EXAFS spectra of P/FeO$_x$ (Fig. 2f) display contour intensity maxima at 4.23 Å^{-1} and 7.89 Å^{-1}, closely matching those of FeO$_x$ and Fe$_2$O$_3$, corroborating the above XAS analysis and confirming the structural integrity of the doped catalyst.

The OER performance of P/FeO$_x$ and the reference sample was evaluated in 1 M KOH electrolyte using a standard three-electrode configuration. All catalysts were ultrasonically dispersed for 1 h and then uniformly deposited on 1 × 1 cm^2 nickel foam substrates at a loading of 1 mg cm^{-2} (Fig. 3). As shown in Fig. 3a, the iR-corrected polarization curves demonstrate that P/FeO$_x$ achieves current densities of 10 and 100 mA cm^{-2} at overpotentials of 208 and 256 mV, respectively (Fig. S15, SI). These values are significantly lower than that of FeO$_x$ (258 and 334 mV) and bare nickel foam (293 and 427 mV), outperforming many recently reported OER catalysts (Fig. 3c, S29 and Table S4, SI). To determine the optimal phosphorus feeding ratio, a series of P/FeO$_x$ catalysts with different nominal phosphorus contents of 1, 2, 4, 6, and 8 wt% were synthesized under otherwise identical molten-salt flash synthesis conditions. Representative SEM images show that these samples generally maintain nanoparticle morphologies, suggesting that the overall morphology is mainly governed by the molten-salt reaction environment. Their OER activities were further evaluated in 1.0 M KOH. As shown in Fig. S16 and Table S5, the 2 wt% P/FeO$_x$ sample exhibits the best catalytic performance, with an overpotential of 256 mV at 100 mA cm^{-2}. By contrast, both lower and higher phosphorus contents result in decreased activity. This result indicates that phosphorus incorporation has an optimal range: insufficient phosphorus limits electronic/defect modulation, whereas excessive phosphorus may disturb the optimized surface structure or partially block active sites, leading to inferior OER performance. Given the intrinsically sluggish OER kinetics, Tafel slopes ($\Delta\eta/\Delta\log|j|$) were calculated to assess reaction kinetics. As shown in Fig. 3b, P/FeO$_x$ exhibits an exceptionally low Tafel slope of ∼31.6 mV dec^{-1}, substantially outperforming FeO$_x$ (∼73.9 mV dec^{-1}), and nickel foam (∼50.3 mV dec^{-1}), confirming its superior kinetic characteristics. Electrochemical impedance spectroscopy (EIS) was also employed to further evaluate the charge-transfer resistance (R_{ct}). The Nyquist plots (Fig. S15b, SI) reveal that P/FeO$_x$ possesses the smallest R_{ct} among the tested catalysts, indicating the most efficient interfacial electron-transfer dynamics.

The electrochemical double-layer capacitance (C_{dl}), determined from cyclic voltammetry (CV) tests at varying scan rates (Fig. S17, SI), was used as a proxy for the electrochemically active surface area. As shown in Fig. 3d, P/FeO$_x$ exhibits a markedly larger C_{dl} compared with the control sample, suggesting a higher density of accessible active sites. Catalyst durability was also assessed, as stability is a key performance criterion for OER catalysts. As shown in Fig. 3e, P/FeO$_x$ demonstrates outstanding long-term stability, retaining over 97% of its initial activity after 2000 h of continuous operation at a constant current density of 100 mA cm^{-2}. Moreover, its linear sweep voltammetry (LSV) curve after 18 000 activation cycles nearly overlaps with the initial curve (Fig. 3e), indicating

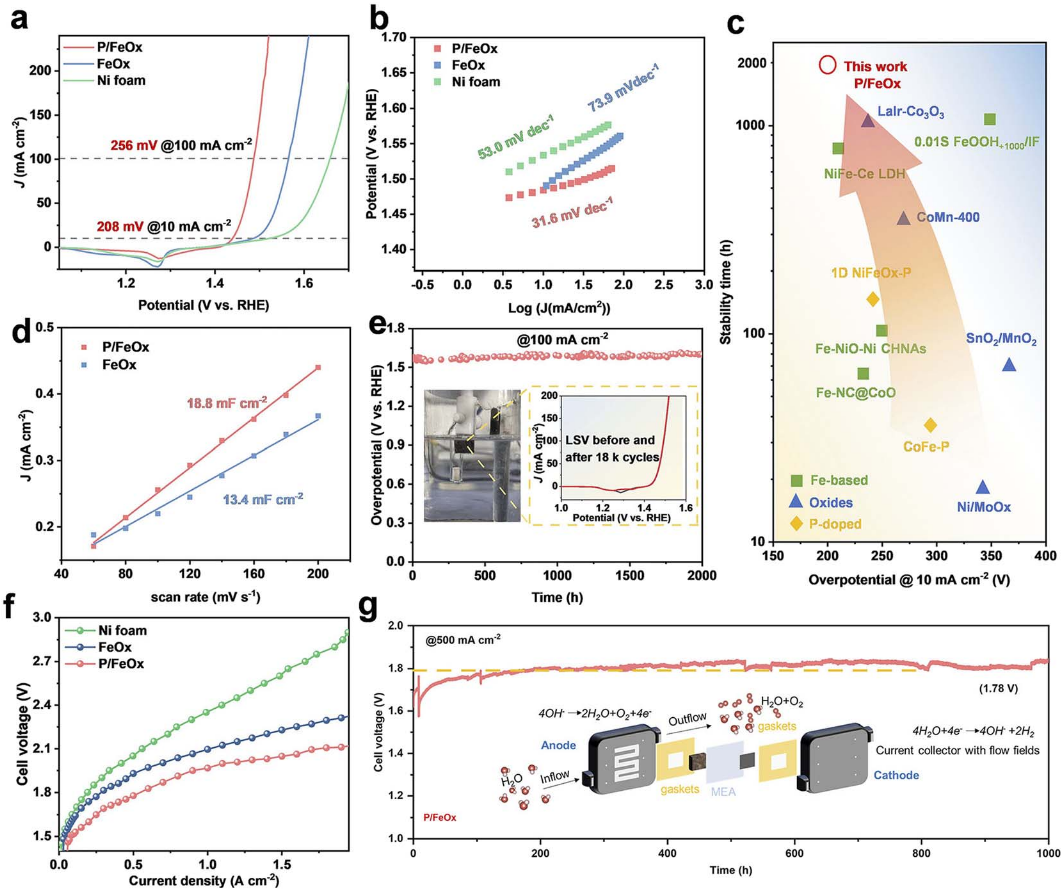

Fig. 3 (a) Polarization curves of P/FeO$_x$, FeO$_x$ and Ni foam measured at a scanning rate of 2 mV s^{-1} in 1 M KOH electrolyte. (b) Tafel slopes of P/FeO$_x$, FeO$_x$ and Ni foam. (c) Values of overpotential and stability hours of recently reported OER catalysts. (d) Double-layer capacitors (C_{dl}) of P/FeO$_x$ and its comparative samples. (e) *E*–*t* curve of P/FeO$_x$ at 100 mA cm^{-2} in 1 M KOH electrolyte. (f) The cell voltage of AEM aqueous electrolyzers based on Pt/C‖P/FeO$_x$, Pt/C‖FeO$_x$ and Pt/C‖Ni foam at 60 °C. (g) *E*–*t* curve of the P/FeO$_x$ loaded AEMWE in 1 M KOH electrolyte at 500 mA cm^{-2}.

negligible degradation. In contrast, FeO$_x$ exhibits an overpotential decay of ~40 mV at 100 mA cm^{-2} after cycling (Fig. S18, SI). To further verify the structural robustness of P/FeO$_x$ under prolonged electrochemical operation, post-cycling characterization studies were carried out after 18 000 LSV cycles. The XRD pattern of the cycled catalyst remains essentially unchanged compared with that of the pristine sample, with no obvious impurity peaks or detectable phase transformation. Furthermore, the post-cycling STEM and TEM images (Fig. S19, SI) show that the nanostructure is largely preserved and clear lattice fringes are still maintained, further confirming the excellent structural stability of P/FeO$_x$ during long-term OER cycling. In addition, XPS analysis after cycling shows that the Fe 2p, O 1s, and P 2p spectra exhibit no significant change compared with those of the fresh sample, and the Fe^{3+} peaks remain nearly unchanged, indicating good stability of the surface chemical states during prolonged electrochemical operation. When benchmarked against state-of-the-art OER catalysts reported in recent literature at 10 mA cm^{-2}, P/FeO$_x$ maintains a clear performance advantage (Fig. S29, SI). Furthermore, faradaic efficiency measurements (Fig. S20, SI) confirm that both doped and undoped catalysts achieve nearly 100% selectivity toward oxygen evolution, indicating that phosphorus incorporation does not induce parasitic side reactions and that the measured current arises exclusively from the OER process.

The synthesized P/FeO$_x$ catalyst was further employed as the anode material in a customized anion exchange membrane water electrolysis (AEMWE) device (Fig. S21, SI). Commercial Pt/C served as the cathode to form the electrode pair (Pt/C‖P/FeO$_x$), while Pt/C‖FeO$_x$ and Pt/C‖Ni foam configurations were used as a benchmark for comparison. The electrolysis performance of the assembled AEMWE systems is shown in Fig. 3f. Polarization measurements reveal that the Pt/C‖P/FeO$_x$ cell achieves cell voltages of 1.51 and 1.76 V at current densities of 100 and 500 mA cm^{-2}, respectively, at 60 °C. These values are significantly lower than those of the FeO$_x$-based electrolyzer (1.63 and 1.93 V at 100 and 500 mA cm^{-2}) and the Ni foam-based one (1.69 and 2.05 V at 100 and 500 mA cm^{-2}), clearly demonstrating the superior catalytic performance of P/FeO$_x$. Moreover, this superior performance surpasses that of most recently reported AEMWE systems (Table S6, SI). Temperature-dependent linear sweep voltammetry (LSV) measurements further confirm that elevated operating temperatures were capable of decreasing the required cell voltage and enhancing catalytic kinetics (Fig. S22, SI). In addition to high activity, the P/FeO$_x$-based AEMWE exhibits excellent durability, maintaining a nearly constant voltage of ∼1.78 V over 1000 h of continuous operation at 500 mA cm^{-2}, with less than 5% performance degradation (Fig. 4g). These results collectively demonstrate the high efficiency and long-term stability of P/FeO$_x$ as a robust anode catalyst for AEMWE, underscoring its strong potential for sustainable, large-scale hydrogen production.

In situ Raman spectroscopy was employed to track the structural evolution of P/FeO$_x$ and FeO$_x$ during the anodic polarization process. At open-circuit potential, both samples exhibit the characteristic spectrum of α-Fe$_2$O$_3$ (218, 286, 400, 488 and 602 cm^{-1}). For P/FeO$_x$, these peaks begin to attenuate at 0.40 V *vs.* RHE and are completely extinguished by 0.60 V (Fig. 4a). The reversible disappearance of Raman intensity is attributed to potential-driven, concerted extraction of lattice oxygen and hole injection into Fe 3d states, which transiently breaks the translational symmetry required for Raman activity without provoking long-range amorphization or cation dissolution. Upon returning the potential to <0.40 V, the original phonon manifold is quantitatively restored, confirming that the Fe–O sublattice remains intact throughout the redox cycle. In contrast, the undoped FeO$_x$ retains its full Raman signature up to 0.50 V and only begins to weaken above 0.60 V (Fig. S23, SI), demonstrating the slow reaction potential of the undoped catalyst.

In our endeavor to delve deeper into the catalyst's active source, we undertook an in-depth investigation into the fundamental mechanisms that govern its activity enhancement and functional performance. The OER generally proceeds through two primary pathways: the adsorbate evolution mechanism (AEM) and the lattice oxygen mechanism (LOM). The key distinction between these two pathways lies in the nature of the reaction intermediates. In the AEM pathway, the OER progresses *via* the formation of the *OOH intermediate, which typically incurs a high overpotential due to the energy-intensive O–O bond formation step. In contrast, the LOM pathway circumvents the *OOH formation by directly coupling *O species with lattice oxygen to generate *OO, thereby reducing the overall energy barrier and facilitating oxygen evolution. To experimentally validate the mechanistic transition, the pH dependence of OER activity was systematically examined. LSV measurements were conducted across a pH range of 12.5–14 (Fig. 4b). As shown in Fig. 4c, P/FeO$_x$ exhibits a markedly stronger pH dependence compared to FeO$_x$. Quantitative analysis based on the proton reaction order ($\rho_{\mathrm{RHE}} = \partial \log j/\partial \mathrm{pH}$, referenced to the reversible hydrogen electrode) yields a ρ_{RHE} value of 0.59 for P/FeO$_x$, substantially higher than those of FeO$_x$

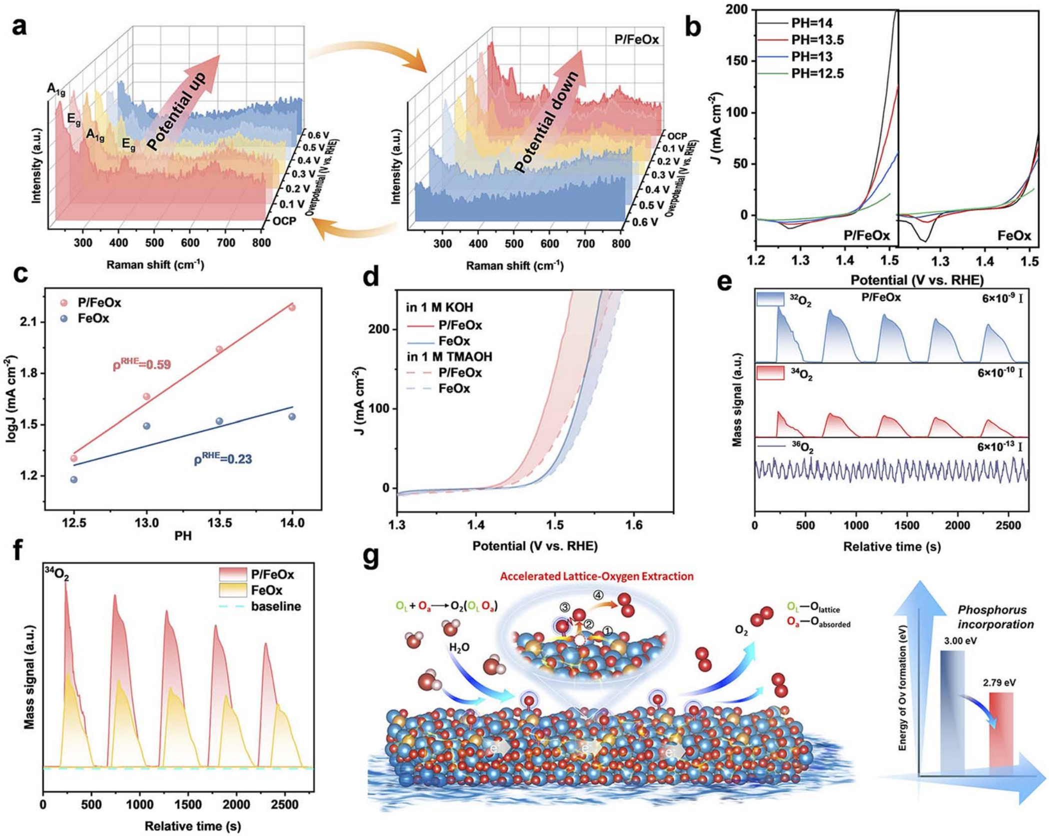

Fig. 4 (a) *In situ* Raman spectra of P/FeO$_x$. (b) Linear sweep voltammetry (LSV) curves of P/FeO$_x$ and FeO$_x$ in KOH solution under different pH conditions. (c) Linear fitting values of pH dependent ρ_{RHE} values for P/FeO$_x$ and its comparison sample. (d) LSV curves of P/FeO$_x$ and its comparative sample in 1 M KOH and 1 M TMAOH. (e) ^{18}O-labeled differential electrochemical mass spectrometry results for P/FeO$_x$ and its (f) signal comparison of ^{34}O with FeO$_x$. (g) Schematic diagram of the accelerated lattice-oxygen extraction process and the energy of O$_v$ formation in P/FeO$_x$ and FeO$_x$ catalysts.

(0.23). This elevated proton reaction order indicates that the OER kinetics of P/FeO$_x$ are strongly influenced by proton activity, consistent with a non-concerted proton–electron transfer process characteristic of the LOM, rather than the conventional AEM pathway.

Direct experimental evidence for LOM participation was further obtained through the detection of negatively charged oxygen intermediates ($^*O_2^{2-}$), which are characteristic of lattice oxygen involvement. Tetramethylammonium hydroxide (TMAOH) was employed as a mechanistic probe, as its cation (TMA$^+$) can electrostatically bind to these negatively charged oxygen species, competitively blocking active sites and suppressing OER activity if the LOM pathway is operative (Fig. 4d). When the electrolyte was switched from 1 M KOH to 1 M TMAOH, P/FeO$_x$ exhibited a pronounced activity loss, requiring an additional 36 mV to reach 100 mA cm^{-2}. In contrast, the overpotentials of FeO$_x$ decreased by only 15 mV. This sharp contrast strongly supports the predominance of the LOM pathway in P/FeO$_x$. Kinetic behavior was further analyzed by examining the redox peaks in the OER pre-regime at scan rates ranging from 1 to 5 mV s^{-1} (Fig. S24, SI). The relationship between peak current (i) and scan rate (v) follows the equation $i = av^b$, where the exponent b (obtained from the slope of log i *versus* $\log v$) reflects the rate-determining process: $b \approx 0.5$ indicates diffusion-controlled behavior, while $b \approx 1.0$ corresponds to surface-capacitive (adsorption-controlled) behavior. Deconvolution of the b values (Fig. S25, SI) reveals that approximately 67% of the OER process on P/FeO$_x$ is governed by surface-capacitive control, with only 33% limited by diffusion. In contrast, FeO$_x$ exhibits significantly lower surface-controlled contributions (45%), indicating that P–O bonding facilitates a transition from diffusion-limited to surface-dominated kinetics. This shift aligns well with the activation of the LOM pathway. To provide mechanistic insight into the involvement of catalyst-derived oxygen species, *operando* ^{18}O-labeled differential electrochemical mass spectrometry (DEMS) measurements were performed using $H_2{}^{18}O$ in 1 M KOH. After ^{18}O labeling, the catalyst was rinsed with $H_2{}^{16}O$ electrolyte five times and then subjected to OER measurements in 1 M $H_2{}^{16}O$, while the evolved oxygen species were continuously monitored by online DEMS. During repeated electrochemical cycling, weakly adsorbed or loosely bound surface ^{18}O species would be expected to be largely consumed at the early stage of the measurement. Therefore, although a minor contribution from surface-exchangeable oxygen species cannot be completely excluded, the stronger $^{16}O^{18}O$ signal observed for P/FeO$_x$ than for FeO$_x$ provides strong evidence for the participation of catalyst-derived oxygen species during the OER and is consistent with enhanced lattice-oxygen involvement. Combined with the pH-dependent behavior, TMAOH probing experiments, and ^{18}O isotope labeling mass spectrometry, these observations support a LOM-involved OER process with increased lattice-oxygen participation in P/FeO$_x$, rather than an exclusive LOM pathway.

The high density of oxygen vacancies, outstanding OER performance, and reduced Tafel slope collectively indicate modified reaction kinetics and the possible involvement of the LOM pathway. The doping approach has proven effective in promoting lattice oxygen release within iron oxide. Phosphorus doping significantly reduces the energy required for the formation of lattice oxygen vacancies. Computational analysis confirmed that the introduction of a single phosphorus atom can decrease the oxygen formation energy from 3.00 eV to 2.79 eV (Fig. 4g). The schematic diagram in Fig. 4g shows that the released lattice oxygen combines with adsorbed oxygen species to form oxygen molecules, thereby completing a full cycle of the LOM pathway. This mechanism not only enhances the catalytic activity of the iron oxide but also offers new perspectives for optimizing OER catalysts.

To further elucidate the origin of the exceptional intrinsic OER activity and durability of P/FeO$_x$, density functional theory (DFT) calculations were conducted to comprehensively investigate its reaction mechanism. To reflect the experimentally observed surface-doped character of P/FeO$_x$, the DFT calculations were performed on a defective α-Fe_2O_3 (012) slab in which the P atom was introduced only into the outermost surface layer. The corresponding model contains one surface oxygen vacancy and a surface P concentration of one P atom per 109.14 Å^2. This model reasonably captures the surface-confined phosphorus modification and was used to evaluate its influence on the electronic structure and OER energetics (Fig. S27, SI). In the lattice oxygen mechanism, lattice oxygen directly participates in the OER as part of the reaction intermediates, and the direct O–O coupling effectively circumvents the linear scaling relationship that constrains the conventional adsorbate evolution mechanism. The optimized structural model and the corresponding reaction pathway are illustrated in Fig. 5a. A comparative analysis of the density of states (DOS) for P/FeO$_x$ and FeO$_x$ (Fig. 5b and c) reveals that FeO$_x$ possesses a bandgap of 1.24 eV between the Fe 3d and O 2p states. Upon the co-introduction of nonmetallic phosphorus and oxygen vacancies (O$_v$), the valence and conduction bands begin to overlap, effectively eliminating the bandgap. This overlap signifies enhanced electronic coupling between the Fe 3d and O 2p orbitals, thereby promoting charge delocalization and improving electrical conductivity. To gain deeper mechanistic insight into the LOM-driven OER process, Gibbs free energy (ΔG) profiles for each elementary step were computed for Fe active sites (Fig. 5d). For both P/FeO$_x$ and FeO$_x$, the potential-determining step corresponds to the dehydrogenation of adsorbed *OH to *O. Notably, phosphorus doping and oxygen-vacancy formation substantially lower the ΔG for this step from 1.15 to 0.89 eV, underscoring the crucial role of phosphorus in facilitating *OH dehydrogenation.

To further probe the electronic origin of this enhancement, adsorption configurations of OH* on FeO$_x$ and P/FeO$_x$ were analyzed through differential charge density mapping (Fig. 5e). In FeO$_x$–OH*, a charge of 0.32 eV is transferred from the catalyst to the OH* adsorbate, whereas this value increases to 0.35 eV in P/FeO$_x$–OH*. Since the oxygen atom in OH* is directly bonded to the active Fe site, the increased electron density localized on this oxygen enhances electrostatic repulsion toward the positively charged H*, thereby promoting H* desorption. The strength of the O–H bond was further evaluated using projected crystal orbital Hamilton population (pCOHP) analysis. The

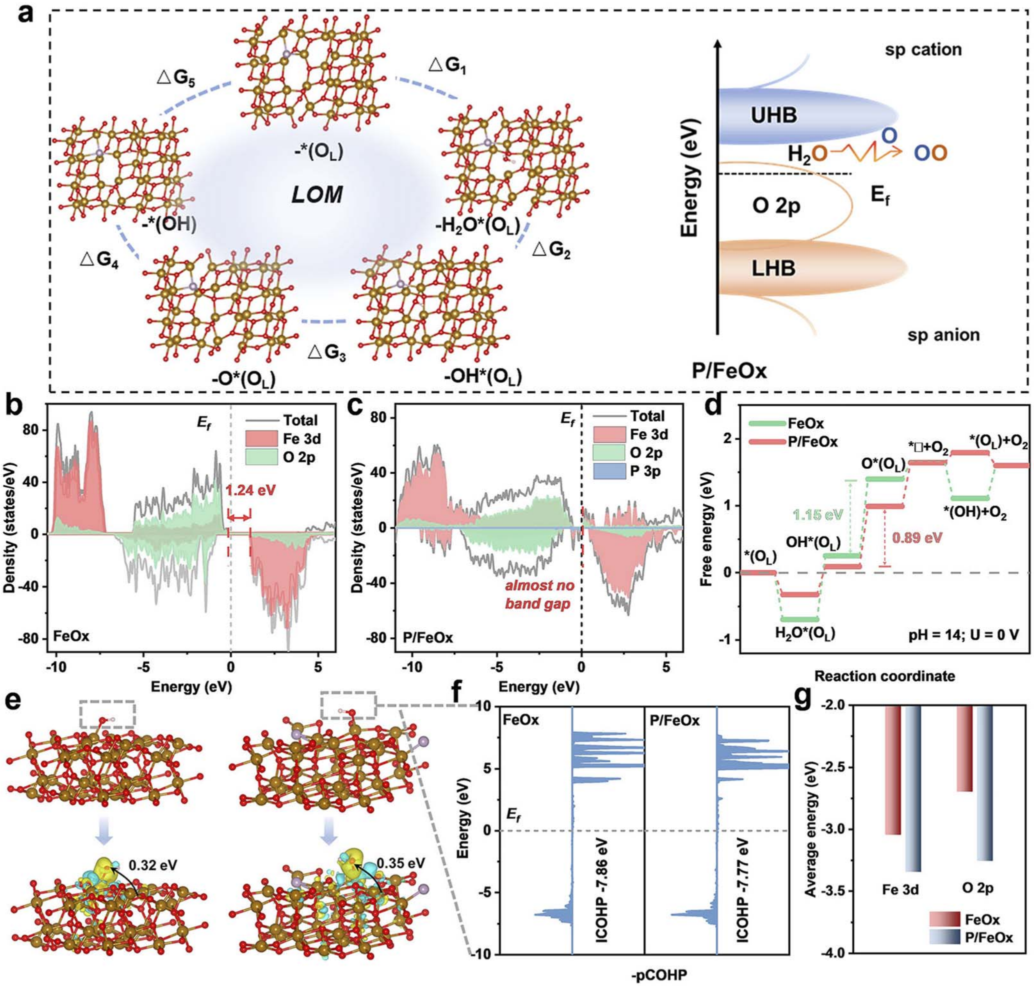

Fig. 5 (a) Schematic diagram of the catalyst's LOM reaction. (b) TDOS diagram of FeO_x. (c) TDOS diagram of P/FeO_x. (d) Step diagrams of P/FeO_x and its comparative sample at pH = 14 and $U = 0$ V. (e) Bader charge distribution diagram. (f) PCOHP plots of P/FeO_x–OH and its comparison sample. (g) Bar chart of d-band center changes in the Fe 3d and O 2p orbitals of P/FeO_x and FeO_x catalysts.

integrated COHP value for the O–H bond increases from −7.86 to −7.77 upon phosphorus and oxygen-vacancy incorporation (Fig. 5f), indicating a weakened O–H bond and a reduced energy barrier for dehydrogenation. Moreover, d-band center calculations (Fig. 5g and S28, SI) reveal that phosphorus and O_v co-doping downshifts the O 2p band center from −2.70 to −3.26 eV. This downward shift was consistent with the electron-donating characteristics of phosphorus and oxygen vacancies. The enhanced O 2p antibonding state further weakens the generated O–H bond, promoting the cleavage of the O–H bond during the dehydrogenation process.

Conclusions

In summary, we have developed a high-performance FeO_x-based OER catalyst through a rapid molten-salt-assisted synthesis approach. Strategic phosphorus doping enables precise regulation of oxygen vacancies and fine-tuning of the local electronic environment around Fe centers. The resulting P/FeO_x catalyst exhibits remarkable OER activity, reducing the overpotential at 100 mA cm^{-2} from 334 to 256 mV while maintaining outstanding durability over 2000 hours of continuous operation. When integrated into an anion exchange membrane water electrolyzer, the catalyst achieves a low cell voltage of 1.78 V at 500 mA cm^{-2} (60 °C) and demonstrates stable operation for over 1000 h. Density functional theory calculations reveal that phosphorus incorporation and oxygen vacancies synergistically narrow the Fe 3d–O 2p bandgap, enhance electronic conductivity, and lower the activation barrier for the rate-determining OH* → O* step, thereby enabling highly efficient and durable OER catalysis. Based on these findings, this study establishes a facile, efficient synthesis strategy readily scalable to kilogram quantities, offering practical guidelines for expedited development of high-performance oxygen evolution electrocatalysts in industrial water electrolysis.

Experimental section

Chemicals and reagents

Potassium hydroxide (KOH, 95%), sodium nitrate ($NaNO_3$, AR, 99.0%), platinum on carbon (Pt/C) and methanol (AR) were obtained from Aladdin Biochemical Technology Co., Ltd.

Sodium dihydrogen phosphate (NaH_2PO_4, 99.9%) was purchased from Macklin Biochemical Technology Co. Ferrous chloride ($FeCl_2$, AR) was obtained from Xi'an Tianmao Chemical Co., Ltd.

Material synthesis

All syntheses employed a KSL-1200X muffle furnace (MTI Corp.) for heat treatment and a Cence Xiangyi H1850 centrifuge for solid–liquid separation. Firstly, 4 g $NaNO_3$ was finely ground in an agate mortar, transferred to a 50 mL alumina crucible, and ramped at 10 °C min^{-1} to 350 °C under static air. A muffle furnace can hold 6–7 crucibles for simultaneous reactions. Then, 150 mg $FeCl_2$, 8 mg NaH_2PO_4 and 1 g $NaNO_3$ were ground evenly and quickly added to the molten salt. After reacting for 3 min, the crucible was removed from the furnace and quenched to room temperature. The solidified product was dissolved in deionized water and centrifuged at 10 800 rpm for 3 min. The pellet was re-dispersed and washed twice more to eliminate residual $NaNO_3$ and chloride. The final precipitate was dried overnight at 60 °C under dynamic vacuum ($<10^{-2}$ mbar) to yield the red P/FeO_x powder.

FeO_x was prepared identically by omitting NaH_2PO_4 entirely, while all other parameters remained unchanged.

Author contributions

J.-H. Luo was responsible for conceptualization, methodology, investigation, data curation, and writing the original draft. B.-X. Wu and K.-J. Yan contributed to the formal analysis, validation, and visualization of the data and reviewing and editing of the manuscript. Y.-B. Mu, Q. Zhang, H.-X. Zou, Z.-Q. Tang, G.-B. Zhang and W. Limphirat were responsible for the characterization of materials. L. Zeng and W.-J Li served as the corresponding authors and were responsible for project administration, supervision, funding acquisition, and final approval of the manuscript for submission. All authors discussed the results and commented on the manuscript.

Conflicts of interest

The authors declare no conflict of interest.

Data availability

The data supporting this article have been included as part of the supplementary information (SI). Supplementary information: experimental details, materials characterization data, electrochemical measurements, and supplementary discussion. See DOI: https://doi.org/10.1039/d6sc02442d.

Acknowledgements

This work was financially supported by the Guangdong Major Project of Basic Research (No. 2023B0303000002), Guangdong Basic and Applied Basic Research Foundation (No. 2022B1515120004), Shenzhen Science and Technology Plan Project (No. KCXST20221021111406016) and High Level of Special Funds (G03034K001).

Notes and references

1 W. Li, Y. Ding, Y. Zhao, Z. Li, G. Lin, L. Wang and L. Sun, Zwitterion-Modified NiFe OER Catalyst Achieving Ultra-Stable Anion Exchange Membrane Water Electrolysis via Dynamic Alkaline Microenvironment Engineering, *Angew. Chem.*, 2025, **137**, e202505924.

2 S. Pan, H. Li, T. Wang, Y. Fu, S. Wang, Z. Xie, L. Wei, H. Li and N. Li, Er-Doping Enhances the Oxygen Evolution Performance of Cobalt Oxide in Acidic Medium, *ACS Catal.*, 2024, **14**(18), 13814–13824.

3 G. Ding, H. Lee, Z. Li, J. Du, L. Wang, D. Chen and L. Sun, Highly Efficient and Durable Anion Exchange Membrane Water Electrolyzer Enabled by a Fe-Ni_3S_2 Anode Catalyst, *Adv. Energy Sustain. Res.*, 2023, **4**(1), 2200130.

4 Y. Ren, C. Song, H. Wang and Z. Qu, Accelerated Dual Activation of Lattice Oxygen and Molecule Oxygen over $CoMn_2O_4$ Catalysts for Voc Oxidation: Promoting the Role of Oxygen Vacancies, *ACS Catal.*, 2024, **14**(6), 4340–4351.

5 T. Jiang, X. Jiang, C. Jiang, J. Wang, Y. Danlos, T. Liu, C. Deng, C. Chen, H. Liao and V. Kyriakou, Novel Fe-Modulating Raney-Ni Electrodes toward High-Efficient and Durable AEM Water Electrolyzer, *Adv. Energy Mater.*, 2025, **15**, 2501634.

6 H. J. Zhang, Z. Q. Chen, X. T. Ye, K. Xiao and Z. Q. Liu, Electron Delocalized Ni Active Sites in Spinel Catalysts Enable Efficient Urea Oxidation, *Angew. Chem., Int. Ed.*, 2025, **64**, e202421027.

7 D. Xu, M. B. Stevens, M. R. Cosby, S. Z. Oener, A. M. Smith, L. J. Enman, K. E. Ayers, C. B. Capuano, J. N. Renner and N. Danilovic, Earth-Abundant Oxygen Electrocatalysts for Alkaline Anion-Exchange-Membrane Water Electrolysis: Effects of Catalyst Conductivity and Comparison with Performance in Three-Electrode Cells, *ACS Catal.*, 2018, **9**(1), 7–15.

8 Y. Zi, C. Zhang, J. Zhao, Y. Cheng, J. Yuan and J. Hu, Research Progress in Structure Evolution and Durability Modulation of Ir- and Ru-Based OER Catalysts under Acidic Conditions, *Small*, 2024, **20**(50), 2406657.

9 W. Kuang, Z. Cui, C. Wang, T. Chen, Q. Wang, S. Li, T. Yang and J. Liu, Self-Supported Ni/$Ni(OH)_2$ Electrodes for High-Performance Alkaline and AEM Water Electrolysis, *Adv. Energy Mater.*, 2025, **15**(14), 2406080.

10 M. Klingenhof, H. Trzesniowski, S. Koch, J. Zhu, Z. Zeng, L. Metzler, A. Klinger, M. Elshamy, F. Lehmann and P. Buchheister, High-Performance Anion-Exchange Membrane Water Electrolysers Using NiX (X = Fe, Co, Mn) Catalyst-Coated Membranes with Redox-Active Ni–O Ligands, *Nat. Catal.*, 2024, **7**(11), 1213–1222.

11 C. Hou, L. Xue, L. Zhou, C. Chen, X. Lv and J. Dang, Efficient Stainless Steel-Based Bifunctional Water Electrolysis Electrode: Activating the OPM Mechanism in OER and Enhancing HER Performance, *Acta Mater.*, 2025, **297**, 121361.

12 J. Tang, X. Xu, T. Tang, Y. Zhong and Z. Shao, Perovskite-Based Electrocatalysts for Cost-Effective Ultrahigh-Current-Density Water Splitting in Anion Exchange Membrane Electrolyzer Cell, *Small Methods*, 2022, **6**, 2201099.

13 J. W. Li, Z. Q. Ge, H. J. Zhang, S. P. Jiang and Z. Q. Liu, Bandgap-Broken Fe Spinel Electrocatalyst Enables Integrated Seawater Electrolysis, *Angew. Chem., Int. Ed.*, 2026, **65**, e21993.

14 H. Liu, A. Wang, M. Wang, Z. Li, Q. Dai, S. Sun, X. Wang, K. Zhang and L. Wei, One-Step Synthesis of TiO_2/FeO(OH) Nano-Heterostructures as Electrocatalysts for the Oxygen Evolution Reaction, *ACS Appl. Nano Mater.*, 2024, **7**(23), 27408–27417.

15 L. Wu, M. Ning, X. Xing, Y. Wang, F. Zhang, G. Gao, S. Song, D. Wang, C. Yuan and L. Yu, Boosting Oxygen Evolution Reaction of (Fe,Ni)OOH via Defect Engineering for Anion Exchange Membrane Water Electrolysis under Industrial Conditions, *Adv. Mater.*, 2023, **35**(44), 2306097.

16 K. Zhang and R. Zou, Advanced Transition Metal-Based OER Electrocatalysts: Current Status, Opportunities, and Challenges, *Small*, 2021, **17**(37), 2100129.

17 L. Yang, R. He, M. Botifoll, Y. Zhang, Y. Ding, C. Di, C. He, Y. Xu, L. Balcells and J. Arbiol, Enhanced Oxygen Evolution and Zinc-Air Battery Performance via Electronic Spin Modulation in Heterostructured Catalysts, *Adv. Mater.*, 2024, **36**(31), 2400572.

18 F. He, Q. Zheng, X. Yang, L. Wang, Z. Zhao, Y. Xu, L. Hu, Y. Kuang, B. Yang and Z. Li, Spin-State Modulation on Metal-Organic Frameworks for Electrocatalytic Oxygen Evolution, *Adv. Mater.*, 2023, **35**(41), 2304022.

19 H. Adamu, S. I. Abba, P. B. Anyin, Y. Sani, Z. H. Yamani and M. Qamar, Tuning OER Electrocatalysts toward LOM Pathway through the Lens of Multi-Descriptor Feature Selection by Artificial Intelligence-Based Approach, *ACS Mater. Lett.*, 2022, **5**(2), 299–320.

20 A. Grimaud, O. Diaz-Morales, B. Han, W. T. Hong, Y. L. Lee, L. Giordano, K. A. Stoerzinger, M. T. Koper and Y. Shao-Horn, Activating Lattice Oxygen Redox Reactions in Metal Oxides to Catalyse Oxygen Evolution, *Nat. Chem.*, 2017, **9**(5), 457–465.

21 R. Chen, Z. Wang, S. Chen, W. Wu, Y. Zhu, J. Zhong and N. Cheng, Activating Lattice Oxygen in Spinel Oxides via Engineering Octahedral Sites for Oxygen Evolution, *ACS Energy Lett.*, 2023, **8**(8), 3504–3511.

22 S. Ni, H. Qu, Z. Xu, X. Zhu, H. Xing, L. Wang, J. Yu, H. Liu, C. Chen and L. Yang, Interfacial Engineering of the $NiSe_2$/$FeSe_2$ p-p Heterojunction for Promoting Oxygen Evolution Reaction and Electrocatalytic Urea Oxidation, *Appl. Catal. B Environ.*, 2021, **299**, 120638.

23 S. Zou, M. S. Burke, M. G. Kast, J. Fan, N. Danilovic and S. W. Boettcher, Fe (Oxy) Hydroxide Oxygen Evolution Reaction Electrocatalysis: Intrinsic Activity and the Roles of Electrical Conductivity, Substrate, and Dissolution, *Chem. Mater.*, 2015, **27**(23), 8011–8020.

24 B. Tian, H. Shin, S. Liu, M. Fei, Z. Mu, C. Liu, Y. Pan, Y. Sun, W. A. Goddard III and M. Ding, Double-Exchange-Induced in Situ Conductivity in Nickel-Based Oxyhydroxides: An Effective Descriptor for Electrocatalytic Oxygen Evolution, *Angew. Chem., Int. Ed.*, 2021, **60**(30), 16448–16456.

25 T. Jiang, X. Jiang, V. Kyriakou, K. Bouzek and H. Liao, Deep Reconstruction of Ni-Al-Based Pre-Catalysts for a Highly Efficient and Durable Anion-Exchange Membrane (AEM) Electrolyzer, *J. Mater. Chem. A*, 2023, **11**(47), 26011–26022.

26 J. S. Ha, Y. Park, J. Y. Jeong, S. H. Lee, S. J. Lee, I. T. Kim, S. H. Park, H. Jin, S. M. Kim and S. Choi, Solar-Powered AEM Electrolyzer via PGM-Free (Oxy)Hydroxide Anode with Solar to Hydrogen Conversion Efficiency of 12.44%, *Adv. Sci.*, 2024, **11**(25), 2401782.

27 X. Li, C. Deng, Y. Kong, Q. Huo, L. Mi, J. Sun, J. Cao, J. Shao, X. Chen and W. Zhou, Unlocking the Transition of Electrochemical Water Oxidation Mechanism Induced by Heteroatom Doping, *Angew. Chem., Int. Ed.*, 2023, **62**(40), e202309732.

28 Y. S. Park, F. Liu, D. Diercks, D. Braaten, B. Liu and C. Duan, High-Performance Anion Exchange Membrane Water Electrolyzer Enabled by Highly Active Oxygen Evolution Reaction Electrocatalysts: Synergistic Effect of Doping and Heterostructure, *Appl. Catal. B Environ.*, 2022, **318**, 121824.

29 L. Tang, T. Fan, Z. Chen, J. Tian, H. Guo, M. Peng, F. Zuo, X. Fu, M. Li and Y. Bu, Binary-Dopant Promoted Lattice Oxygen Participation in OER on Cobaltate Electrocatalyst, *Chem. Eng. J.*, 2021, **417**, 129324.

30 W. Ma, Y. Zhang, B. Wang, J. Wang, Y. Dai, L. Hu, X. Lv and J. Dang, Significantly Enhanced OER and HER Performance of NiCo-LDH and NiCoP under Industrial Water Splitting Conditions through Ru and Mn Bimetallic Co-Doping Strategy, *Chem. Eng. J.*, 2024, **494**, 153212.

31 L. He, N. Wang, M. Xiang, L. Zhong, S. Komarneni and W. Hu, S-Vacancy-Rich NiFe-S Nanosheets Based on a Fully Electrochemical Strategy for Large-Scale and Quasi-Industrial OER Catalysts, *Appl. Catal. B Environ. Energy*, 2024, **345**, 123686.

32 J. C. Gan, Z. F. Jiang, K. M. Fang, X. S. Li, L. Zhang, J. J. Feng and A. J. Wang, Low Rh Doping Accelerated HER/OER Bifunctional Catalytic Activities of Nanoflower-Like Ni-Co Sulfide for Greatly Boosting Overall Water Splitting, *J. Colloid Interface Sci.*, 2025, **677**, 221–231.

33 X. Wang, H. Zhong, S. Xi, W. S. V. Lee and J. Xue, Understanding of Oxygen Redox in the Oxygen Evolution Reaction, *Adv. Mater.*, 2022, **34**(50), 2107956.

34 X. Ren, Y. Zhai, N. Yang, B. Wang and S. Liu, Lattice Oxygen Redox Mechanisms in the Alkaline Oxygen Evolution Reaction, *Adv. Funct. Mater.*, 2024, **34**(32), 2401610.

35 Y. Zhou, J. Zeng, X. Zheng, W. Huang, Y. Dong, J. Zhang, Y. Deng and R. Wu, Enhancing the Oxygen Evolution Reaction Activity and Stability of High-Valent CoOOH by Switching the Catalytic Pathway through Doping Low-Valent Cu, *J. Colloid Interface Sci.*, 2025, **678**, 536–546.

36 J. Zhang, Y. Jin, Z. Xu, Y. Du, Y. Xu, X. Ren, B. Xue, D. Liu, Y. Zhu and F. A. Li, Sol-Gel-Hydrothermal Interfacial Regulation Strategy for Sulfate Intercalation in NiFe-LDH to Promote High-Valent Ni Formation and LOM-Type OER, *ACS Sustainable Chem. Eng.*, 2025, **13**, 15177–15188.

37 Y. Zhu, Y. Zhao, C. Xi, K. Hu, S. Han and J. Jiang, Cationic Defect Engineering Induces LOM-Enhanced Electrocatalysts Derived from in Situ Semi-Transformed NiFe-LDH/MOF Heterostructure for Efficient Overall Water-Splitting, *Composites, Part B*, 2025, **298**, 112356.

38 Q. Deng, H. Li, K. Pei, L. W. Wong, X. Zheng, C. S. Tsang, H. Chen, W. Shen, T. H. Ly and J. Zhao, Strategic Design for High-Efficiency Oxygen Evolution Reaction (OER) Catalysts by Triggering Lattice Oxygen Oxidation in Cobalt Spinel Oxides, *ACS Nano*, 2024, **18**(49), 33718–33728.

39 Q. Huang, G. J. Xia, B. Huang, D. Xie, J. Wang, D. Wen, D. Lin, C. Xu, L. Gao and Z. Wu, Activating Lattice Oxygen by a Defect-Engineered Fe_2O_3-CeO_2 Nano-Heterojunction for Efficient Electrochemical Water Oxidation, *Energy Environ. Sci.*, 2024, **17**(14), 5260–5272.

40 X. Wang, J. Hu, T. Lu, H. Wang, D. Sun, Y. Tang, H. Li and G. Fu, Importing Atomic Rare-Earth Sites to Activate Lattice Oxygen of Spinel Oxides for Electrocatalytic Oxygen Evolution, *Angew. Chem., Int. Ed.*, 2025, **64**(3), e202415306.

41 Z. Q. Chen, W. J. Cai, H. J. Zhang, K. Xiao, B. L. Huang and Z. Q. Liu, Spin Polarization Induced Rapid Reconstruction of Transition Metal Oxide for Efficient Water Electrolysis, *Chem. Sci.*, 2025, **16**, 14750–14759.

42 K. Xiao, Y. F. Wang, P. Y. Wu, L. P. Hou and Z. Q. Liu, Activating Lattice Oxygen in Spinel $ZnCo_2O_4$ through Filling Oxygen Vacancies with Fluorine for Electrocatalytic Oxygen Evolution, *Angew. Chem., Int. Ed.*, 2023, **62**, e202301408.

43 Y. Pan, X. Xu, Y. Zhong, L. Ge, Y. Chen, J.-P. M. Veder, D. Guan, R. O'Hayre, M. Li and G. Wang, Direct Evidence of Boosted Oxygen Evolution over Perovskite by Enhanced Lattice Oxygen Participation, *Nat. Commun.*, 2020, **11**(1), 2002.

44 X. Xu, Y. Pan, Y. Zhong, C. Shi, D. Guan, L. Ge, Z. Hu, Y. Y. Chin, H. J. Lin and C. T. Chen, New Undisputed Evidence and Strategy for Enhanced Lattice-Oxygen Participation of Perovskite Electrocatalyst through Cation Deficiency Manipulation, *Adv. Sci.*, 2022, **9**(14), 2200530.

45 D. Chen and S. Mu, Molten Salt-Assisted Synthesis of Catalysts for Energy Conversion, *Adv. Mater.*, 2024, **36**(45), 2408285.

46 J. Ding, L. Chen and X. Zhu, Molten Salt Synthesis of Low-Dimensional Nanostructured Perovskite Oxide Electrocatalysts for Oxygen Evolution Reaction: A Review, *J. Mater. Chem. A*, 2025, **13**, 37762–37788.

47 Y. N. Zhou, F. L. Wang, S. Y. Dou, Z. N. Shi, B. Dong, W. L. Yu, H. Y. Zhao, F. G. Wang, J. F. Yu and Y. M. Chai, Motivating High-Valence Nb Doping by Fast Molten Salt Method for NiFe Hydroxides toward Efficient Oxygen Evolution Reaction, *Chem. Eng. J.*, 2022, **427**, 131643.

48 J. Wang, J. Yu, X. Chen, Z. Zeng, S. He, H. Liu, Z. Du and Z. Hua, Dual Electronic and Structural Engineering of Ni-Fe Alloys via Molten Salt Electrodeposition for Enhanced Oxygen Evolution Reaction, *Adv. Funct. Mater.*, 2025, e12333.